

# UC Irvine

## UC Irvine Previously Published Works

### Title

Observation of ocean tides below the Filchner and Ronne Ice Shelves, Antarctica, using synthetic aperture radar interferometry: Comparison with tide model predictions

### Permalink

<https://escholarship.org/uc/item/77j3h6dm>

### Journal

Journal of Geophysical Research: Oceans, 105(C8)

### Authors

Rignot, E  
Padman, L  
MacAyeal, DR  
[et al.](#)

### Publication Date

2000-08-15

### DOI

10.1029/1999jc000011

### Copyright Information

This work is made available under the terms of a Creative Commons Attribution License, available at <https://creativecommons.org/licenses/by/4.0/>

Peer reviewed

# Observation of ocean tides below the Filchner and Ronne Ice Shelves, Antarctica, using synthetic aperture radar interferometry: Comparison with tide model predictions

E. Rignot,<sup>1</sup> L. Padman,<sup>2</sup> D. R. MacAyeal,<sup>3</sup> and M. Schmeltz<sup>1</sup>

**Abstract.** Tides near and under floating glacial ice, such as ice shelves and glacier termini in fjords, can influence heat transport into the subice cavity, mixing of the under-ice water column, and the calving and subsequent drift of icebergs. Free-surface displacement patterns associated with ocean variability below glacial ice can be observed by differencing two synthetic aperture radar (SAR) interferograms, each of which represents the combination of the displacement patterns associated with the time-varying vertical motion and the time-independent lateral ice flow. We present the pattern of net free-surface displacement for the iceberg calving regions of the Ronne and Filchner Ice Shelves in the southern Weddell Sea. By comparing SAR-based displacement fields with ocean tidal models, the free-surface displacement variability for these regions is found to be dominated by ocean tides. The inverse barometer effect, i.e., the ocean's isostatic response to changing atmospheric pressure, also contributes to the observed vertical displacement. The principal value of using SAR interferometry in this manner lies in the very high lateral resolution (tens of meters) obtained over the large region covered by each SAR image. Small features that are not well resolved by the typical grid spacing of ocean tidal models may contribute to such processes as iceberg calving and cross-frontal ventilation of the ocean cavity under the ice shelf.

## 1. Introduction

Synthetic aperture radar (SAR) interferometry is a remote sensing technique used to measure displacements of stable, radar reflective portions of the Earth's surface over periods ranging from days to weeks [Gabriel *et al.*, 1989]. The potential for monitoring ice sheet motion with this technique was described by Goldstein *et al.* [1993], who noted that a major contribution to displacements of floating ice sheets was the vertical motion forced by the ocean tides in the cavity under the ice. Hartl *et al.* [1994] developed this idea further by comparing ocean tide height predictions with the displacement evaluated from differencing two SAR interferograms for a single location near the eastern end of the Ronne Ice Shelf in the southern Weddell Sea. The agreement between the two methods suggested that ice

sheet vertical displacements due to ocean tides could be resolved with SAR interferometry.

In the present study we show that for large regions along the ice fronts of the massive floating ice shelves in the southern Weddell Sea (Figure 1) the spatial distributions of vertical displacements measured using SAR interferometry are strongly correlated with distributions based on numerical ocean tidal models. In moving from the single-point comparisons reported by Hartl *et al.* [1994] and Rignot [1996] to the present study of extensive regions of ice shelf we also demonstrate the method's value in providing more spatial detail of ocean tide variability than is available through classical ocean tide measurement techniques such as moored tide gauges and current meters. SAR-derived data can therefore be used to direct the refinement of tidal models for this region where tides are believed to play a significant role in other oceanic and glaciological processes [Robertson *et al.*, 1998; Makinson and Nicholls, 1999]. We also show that it is theoretically possible to determine ocean tidal constituents from this method alone, although present data availability and satellite orbit characteristics preclude this determination at this time.

While the basic concepts behind the use of SAR interferometry are quite straightforward, care is required in the development and interpretation of interferograms

<sup>1</sup>Jet Propulsion Laboratory, California Institute of Technology, Pasadena.

<sup>2</sup>Earth and Space Research, Seattle, Washington.

<sup>3</sup>The Department of Geophysical Sciences, University of Chicago, Chicago, Illinois.

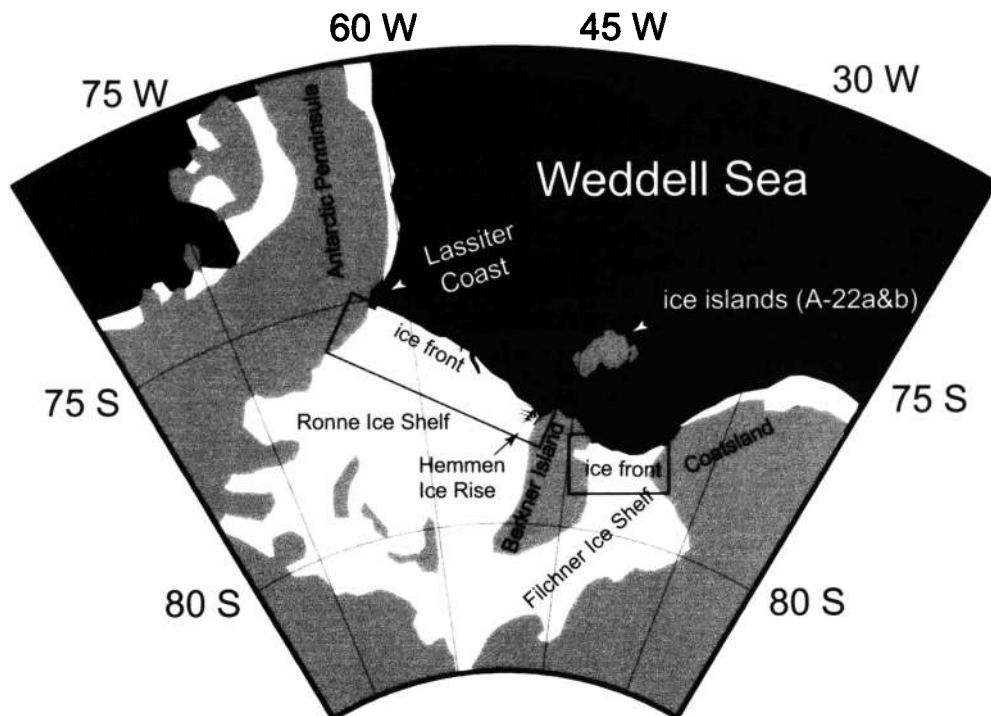


**Figure 1.** Map of the study area (Albers equal area projection). The regions contained within two rectangles denote the approximate coverage of synthetic aperture radar (SAR) interferograms used in this study. Shaded areas represent grounded ice. Black areas represent open water, including regions of seasonal or perennial sea ice. White areas represent floating ice shelf. The ice fronts of the Ronne and Filchner Ice Shelves are depicted approximately in their 1996 configurations. In October of 1998 a large section of the Ronne Ice Shelf calved from the eastern corner near Berkner Island (becoming iceberg A-38), causing the ice front in this area to retreat by ~25 km. The ice front locations in the Grenoble global finite element tidal simulation (FES95.2) and Circum-Antarctic Tidal Simulation (CATS99.4) ocean tide models are located within ~10 km of the 1996 ice front locations shown here. The CATS99.4 model includes three large ice islands north of Berkner Island (shown in shading). The ice islands are tabular icebergs that calved off the Filchner Ice Shelf in 1986 (A-22a and A-22b) and subsequently grounded on the shallow Berkner Bank [Nøst and Østerhus, 1998]. These ice islands were still present in 1996 during the period that the SAR data used in this study were obtained.

for studies of time-dependent processes. Ice shelf surface displacement is actually a blend of tidal and steady creep flow motions [Rignot and MacAyeal, 1998]. To separate tidal from creep displacements, two SAR interferograms are differenced to create what is called a “differential SAR interferogram” (DSI). The unique feature of a DSI is that the differencing operation eliminates displacement patterns that are common to each of the two original interferograms, i.e., time steady ice shelf creep flow. What remains is a “displacement difference” field caused by the tides and any other time-dependent ocean phenomena such as the inverse barometer effect (i.e., ocean response to changing atmospheric pressure), long-period ocean waves, and ocean eddies. (The DSI signal may also include some small instrumental error such as uncompensated changes in the refractive index of the atmosphere.) The two differential interferograms considered in this study are shown in Plates 1 and 2 for the Ronne and Filchner Ice Shelves, respectively.

Conventional sea surface height data usually consist of time series of surface displacements at relatively few

points but sampled sufficiently rapidly to resolve the tides at those points without significant aliasing. In comparison, a differential interferogram reveals a single snapshot of the displacement difference spatial field over some time interval. This field cannot be transformed into the individual displacement fields. However, interferometry does provide extraordinary resolution, accuracy and spatial coverage. The pixel size of a typical SAR interferogram is ~40 m by 40 m, and the accuracy of each displacement measurement is ~1–2 mm, or 2–4% of the radar wavelength (56 mm for ERS-1 and ERS-2). For the two DSIs shown in Plates 1 and 2 the spatial coverage includes the entire width of the southern Weddell Sea, of order 1000 km. This coverage provides simultaneous observation of ocean variability along the entire ice front (i.e., the iceberg calving margin, see Figure 1) of the Ronne and Filchner Ice Shelves (collectively denoted the “FRIS”). These benefits are partly offset by the lack of frequency resolution and the difficulty of separating tidal from nontidal components of ocean height variability with the small number of

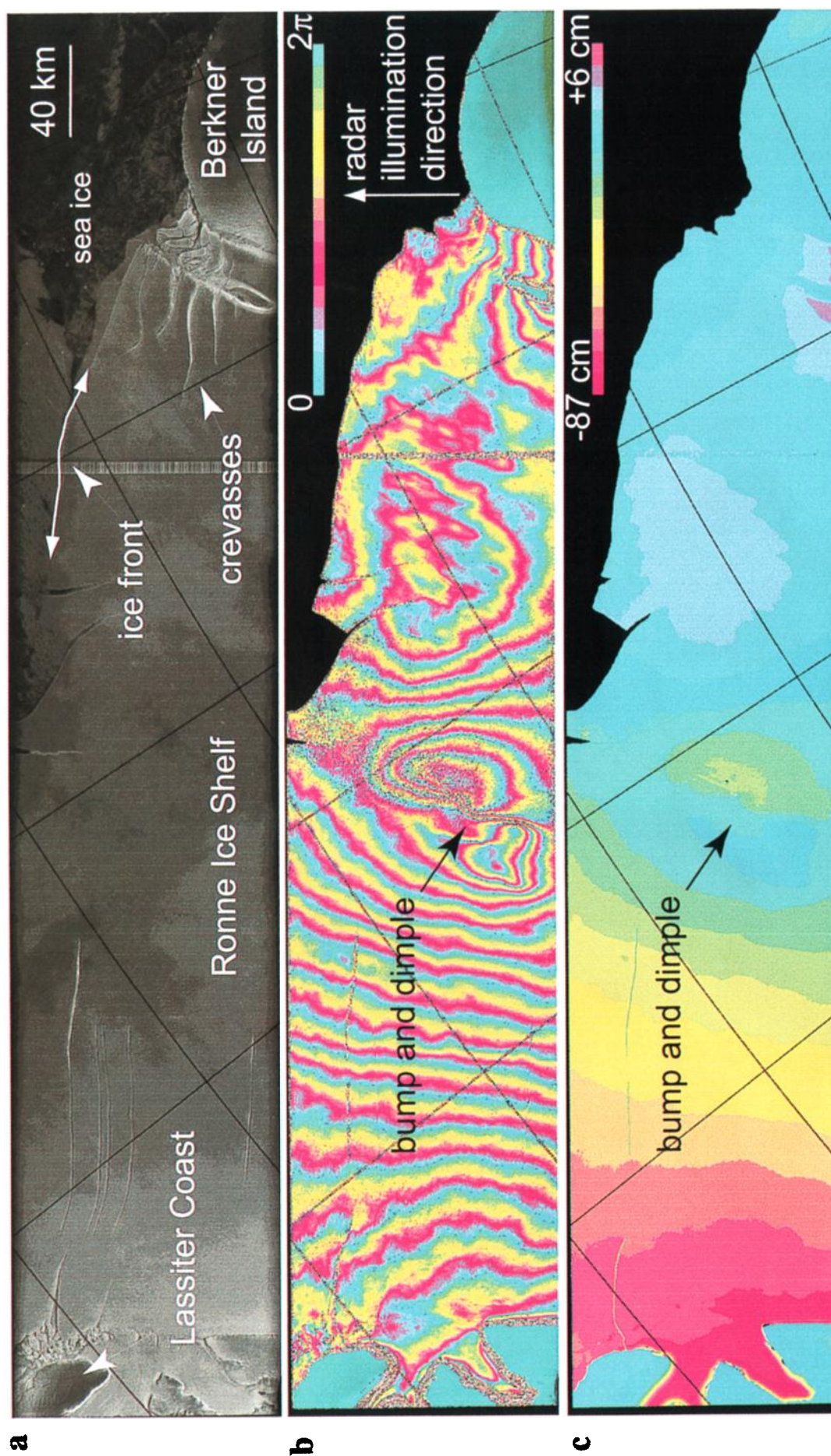


**Plate 1.** (a) SAR amplitude image, (b) fringe pattern, and (c) differential displacement ( $\Delta\eta$ ) for the ice front region of the Ronne Ice Shelf. Each fringe represents a  $2\pi$  difference of phase difference between two separate SAR interferograms. One fringe corresponds to a  $\lambda/2 = 28$  mm range distance difference  $\Delta\zeta$  between the satellite antenna and the surface of the ice shelf ( $\lambda = 56$  mm is the radar wavelength). To convert the fringe pattern to  $\Delta\zeta$ , fringes are counted (using an automatic phase unwrapping algorithm) from a point where  $\Delta\zeta = 0$  (e.g., the grounded portion of Berkner Island).



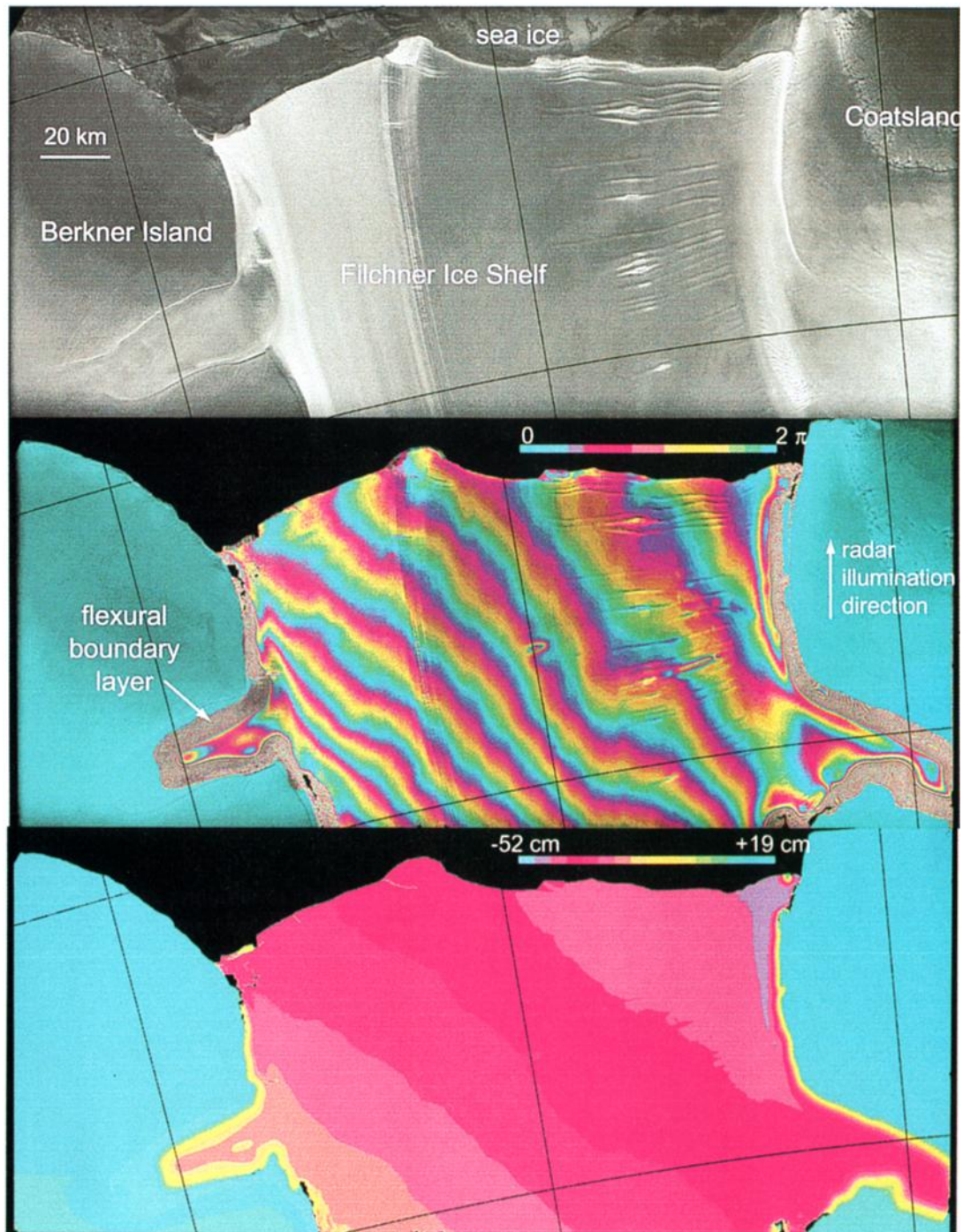


**Plate 2.** (a) SAR amplitude image, (b) fringe pattern, and (c) differential displacement ( $\Delta\eta$ ) of the ice front region of the Filchner Ice Shelf. Along coasts and grounding lines we see a flexural boundary layer identified by the closely spaced, parallel fringe pattern that is  $\sim 9$  km wide [see e.g., Holdsworth, 1977].

DSIs that are likely to be available in the foreseeable future. However, we will show that DSI displacement data help us to identify weaknesses in current numerical ocean tidal models.

Differential interferometry on the FRIS provides the additional benefit of giving tidal information that is complementary to satellite altimetry. For example, the southern Weddell Sea is south of the turning latitude for the TOPEX/Poseidon (T/P) satellite mission, while the

ubiquitous sea ice interferes with the use of altimetry data for obtaining ocean tidal displacements from the ERS satellite missions. The few point measurements in this region are sparsely located because of the logistic difficulty of deploying and recovering instrument moorings, yet we know from numerical models that tidal height and velocity fields here can have small spatial scales and that the spatial variability of tides can play an important role in larger-scale ocean variability

[Makinson, 1997; Robertson *et al.*, 1998; Makinson and Nicholls, 1999; Padman and Kottmeier, 2000].

As an introductory example of the value of DSI, consider the “bump-and-dimple” feature identified in the differential displacement pattern for the Ronne Ice Shelf (Plate 1). Most tidal energy in the Weddell Sea is associated with large-scale Kelvin waves bounded by the Antarctic coastline [Robertson *et al.*, 1998]. These waves have typical length scales of order  $10^3$  to  $10^4$  km, and thus the small scale of the bump-and-dimple is at first surprising. However, tidal models of, and measurements in, the Weddell Sea also identify topographic vorticity waves (TVWs) as components of the total tidal field. TVWs are geostrophically balanced waves that propagate along topographic vorticity gradients (i.e., gradients in  $f/H$ , where  $f$  is the Coriolis parameter and  $H$  is water column thickness) such as the continental slope, the ice front, and various water column thickness structures beneath the ice shelves. (For a map of water-column thickness and bathymetry of the Weddell Sea, see Robertson *et al.* [1998, Figure 1] or the map compiled by Vaughan *et al.* [1994].) The length scales for TVWs are related to topographic scales of variability and, so, can be very small, often  $<100$  km. Modeling of TVWs is difficult for several reasons that are discussed by Padman and Kottmeier [2000]. These reasons include sensitivity of the dispersion characteristics to topographic variability and ocean stratification [Middleton *et al.*, 1987]; and the potential for nonlinear interactions with lower-frequency mean flows [Foldvik *et al.*, 1990]. Diurnal TVWs are known to occur along the southern continental shelf break [see Middleton *et al.*, 1987; Foldvik *et al.*, 1990]. They have not yet been documented along the Ronne or Filchner ice fronts but may explain the bump-and-dimple feature along the Ronne ice front.

In this study we develop the methodology for using differential SAR interferometry to investigate the ocean tide in the ice shelf covered portions of the southern Weddell Sea. We demonstrate that DSI can reveal ice shelf motion due to ocean tides, and that these data can be used to drive future tidal model improvements. Ultimately, data and analyses similar to those presented here are intended to shed light on the time-dependent oceanographic conditions beneath the FRIS and other large ice shelves around Antarctica and to determine the oceanic controls of iceberg calving from Antarctic ice shelves. We first review the SAR data in section 2 and then describe the tidal models used in the comparison with DSIs in section 3. A discussion and summary are provided in sections 4 and 5.

## 2. SAR Data

### 2.1. Summary of SAR Data Acquisition and Analysis

The principal data analysis technique used here involves the construction of differential interferograms as

summarized in section 1. For a more complete description of the theory behind differential interferometry, see Gabriel *et al.* [1989], Hartl *et al.* [1994], Rignot [1996], and Rignot and MacAyeal [1998]. The accuracy and resolution of our data depend on accurate knowledge of the orbital geometry used in the processing of the SAR data. (For a description of the relevant orbital geometry and an analysis of how uncertainty in this geometry affects errors in the interferograms, consult Frolich and Doake [1998].) In the present study we adjusted the orbital geometry, i.e., the interferometric baseline  $B$  defined in Frolich and Doake [1998], so as to remove residual fringe patterns in the grounded ice on either end of the SAR image swaths. (This adjustment requires knowledge of the ice sheet surface elevation, which is provided by the digital elevation model of Bamber and Bindshadler [1997].) As a result of these improvements, we were able to reduce spurious interferometric fringes associated with orbital geometry error in these grounded ice control areas to within interferometric phase noise (i.e., with rms variation within a fraction of a fringe in the DSIs).

SAR data were provided by the European Space Agency (ESA) and collected by ERS-1 and ERS-2. For the two ice shelf regions studied (Figure 1), SAR data from four satellite passes, i.e., two pairs of passes, were used to construct the differential interferograms shown in Plates 1 and 2. Following each pass of the ERS-1 satellite over the sites of interest, the ERS-2 satellite passed over the same sites almost exactly 1 day later. Each pair of ERS-1 and ERS-2 passes was separated by exactly 35 days. Denoting the times of the four satellite passes as  $t_j, j = 1, \dots, 4$ , where  $t_1 < t_2 < t_3 < t_4$ , we note that  $(t_2 - t_1) = (t_4 - t_3) = 24.0$  hours, and  $(t_3 - t_1) = (t_4 - t_2) = 35.0$  days. Accuracy of satellite pass timing is  $\sim 1$  s, and the time differences cited above are within several seconds of being exactly 24.0 hours and 35.0 days. For the Ronne Ice Shelf (Plate 1), the four passes occurred on February 1 and 2 and March 7 and 8, 1996, each near 0555 UTC. For the Filchner Ice Shelf (Plate 2), the four passes occurred on January 15 and 16 and February 19 and 20, 1996, each near 0628 UTC.

The SAR data for each of the two ice shelf regions were processed separately to reveal the “range difference” field,  $\Delta\zeta(\phi, \lambda)$ ,

$$\Delta\zeta(\phi, \lambda) = [\zeta(t_4, \phi, \lambda) - \zeta(t_3, \phi, \lambda)] - [\zeta(t_2, \phi, \lambda) - \zeta(t_1, \phi, \lambda)], \quad (1)$$

where  $\zeta(t_j, \phi, \lambda)$  denotes the range distance between the ice shelf surface and satellite antenna at time  $t_j$ , latitude  $\phi$ , and longitude  $\lambda$ . For a more complete description of the analytical steps needed to generate  $\Delta\zeta$ , see Rignot and MacAyeal [1998].

An essential property of DSI exploited in this study is that  $\Delta\zeta$  depends only on time-dependent motions. We exploit this property to isolate the tidal motion of the ice shelves from the displacements caused by “glacio-

logical” creep flow of the ice shelf, i.e., the quasi-steady horizontal spreading flow caused by gravity (for a description of the ice shelf flow of the FRIS, see *MacAyeal et al.* [1998]). Time dependence in the glaciological creep flow is vanishingly small for large-scale ice shelves in Antarctica and, so, would have an insignificant influence on surface displacements occurring over the 1 day time interval of the two ERS-1 and ERS-2 passes needed to make an interferogram. The most serious concern we had at the outset of our study was the possibility that portions of the FRIS both within and outside the SAR field of coverage could partially ground on the seabed during low tide and that this would cause pulsations of the ice shelf flow during the tidal cycle. Analysis using the ice shelf flow model described by *MacAyeal et al.* [1998], however, suggested that such ice shelf flow pulsations would be small in amplitude and have little influence on the DSI. An area of ephemeral, low-tide grounding in a circular region with a diameter of  $\sim 5$  km in the middle of the region covered by the Filchner Ice Shelf DSI (Plate 2); for example, introduced a creep flow perturbation below  $1 \text{ m a}^{-1}$ . The displacement difference associated with such a small perturbation could not amount to more than a few millimeters even under a worst case scenario, and this would fall well below a single fringe on a DSI. We thus conclude that time-dependent creep flow can be disregarded when considering the influence of the ocean tide and other oceanic processes.

## 2.2. Conversion of SAR Data to Tidal Displacement

For the reasons discussed in Section 2.1 we assume that the glaciological creep flow of both the Filchner and Ronne Ice Shelves is time-independent. With this assumption the observed range difference  $\Delta\zeta$  introduced above may be attributed to sea surface elevation change alone. We convert  $\Delta\zeta$  to a sea surface elevation change  $\Delta\eta$  using

$$\Delta\eta = \frac{\Delta\zeta}{\cos \alpha}, \quad (2)$$

where  $\alpha$  denotes the angle of incidence of the radar illumination with respect to local vertical direction. This angle is calculated assuming a spherical Earth and using the known radar imaging geometry. For ERS-1 and ERS-2,  $\alpha$  is roughly  $23^\circ$  for the Ronne and Filchner images. To evaluate (2), we accounted for the small variations of  $\alpha$  across the region imaged by the SAR. We refer to  $\Delta\eta(\phi, \lambda)$  as the “sea surface displacement change.”

The  $\Delta\eta$  fields for the two ice shelves are shown in Plates 1c and 2c. Several general features are noted. First, there is a large-scale gradient in  $\Delta\eta$  across the two regions, with an elevation difference of up to 60 cm between the Hemmen Ice Rise and Lassiter Coast regions on the Ronne Ice Shelf. This large-scale gradient is consistent with the notion that the ocean tides prop-

agate as Kelvin waves around the coastal margins of the Weddell Sea, including the ocean cavity under the FRIS [*Robertson et al.*, 1998]. A second general feature is the presence of coastal boundary layers that identify elastic flexural interactions between the ice and the tide. As discussed in section 2.1, these boundary layers can be identified by the narrow bands of tightly spaced fringes at the coastline. The width of these layers is typically  $\sim 9$  km (see, e.g., Plate 2), although the exact value depends on variable ice shelf properties such as ice thickness and ice shelf integrity (e.g., the presence of fractures). For large ice shelves the flexural boundary layer is only a small fraction of the total ice shelf area and, so, can be ignored when modeling the ocean tide. For smaller shelves, however, such as the Ekström Ice Shelf [*Riedel et al.*, 2000], the flexural boundary layer can occupy most of the ice shelf area.

## 2.3. Relationship Between Tides and SAR Data

In Appendix A we describe how tidal displacement of the sea surface at the four times of SAR image acquisition determines the DSI-derived  $\Delta\eta$ . Disregarding the influence of error in the DSI data and nontidal ocean processes, the tides uniquely determine the observed  $\Delta\eta$ .

The converse of this statement, that  $\Delta\eta$  uniquely determines the tides, is not true because as described further in Appendix B, the observed  $\Delta\eta$  does not uniquely determine the amplitude and phase of the superimposed tidal constituents. (For a description of the major tidal constituents in the southern Weddell Sea, consult *Robertson et al.* [1998].) Nonuniqueness results from the fact that the 24.0 hour time separation between SAR images (determined by orbit period of the ERS-1 and ERS-2 satellites used to acquire our data) is an exact multiple of the 12.0000 hour period of the semidiurnal solar tide  $S_2$ . In this circumstance the sea surface elevation associated with  $S_2$  is exactly the same each time the SAR satellite passes over a given site. All SAR interferometry acquired by ERS-1 and ERS-2 when orbiting with a 24.0 hour period is thus “blind” to the  $S_2$  tide. Other tidal constituents such as  $K_1$  and  $K_2$  also have periods that are close to being unresolved by the ERS orbits. Given this perspective, plans for future satellite missions carrying SAR sensors must seriously consider tidal sampling problems imposed by the choice of orbit period (see Appendices A and B).

As shown in Appendix A, the primary contribution to the DSI-derived  $\Delta\eta$  comes from tidal constituents  $M_2$  and  $O_1$ , with  $K_1$ ,  $K_2$ ,  $Q_1$ ,  $2N_2$ , and  $N_2$  contributing to a lesser extent. In principle, the amplitude and phase of the “observable” major tidal constituents (i.e., all except  $S_2$ ) can be determined directly from DSI data, using the inversion technique described in Appendix B. The practicality of such an inversion remains suspect, however, because of its requirement for large numbers of independent DSI fields (see Appendix B) to capture

most of the tidal energy and provide some redundancy to permit the removal of nontidal oceanic signals.

Without a direct means of using DSI-derived data to determine the tides we proceed by using comparisons between ocean tide models and DSI fields as a means to understand the implications of the DSI-determined  $\Delta\eta$  fields reported here.

### 3. Ocean Tide Model Predictions

Tidal simulations of the Weddell Sea include regional models developed by *Smithson et al.* [1996], *Robertson et al.* [1998], and *Makinson and Nicholls* [1999], and the Grenoble global finite element tidal simulation (FES95.2) [see *Le Provost et al.* 1998]. All models show the same basic features, with diurnal and semidiurnal Kelvin waves propagating from east to west around the Antarctic continent. The two principal semidiurnal constituents,  $M_2$  and  $S_2$ , have amphidromic points near the Ronne ice front [see *Robertson et al.* 1998, Plate 1] (see also Plate 3). However, the models differ from each other in significant ways, particularly in the diurnal constituents. As mentioned earlier, much of the diurnal tidal energy in the southern Weddell Sea is associated with TVWs rather than basin-scale Kelvin waves. The TVWs are most obvious in maps of tidal kinetic energy but also contribute to the potential energy (sea surface elevation) field and are difficult to model accurately [Padman et al., 1998; Padman and Kottmeier, 2000].

A satisfactory comparison between DSI and any specific model allows us to conclude that the information contained within the observed  $\Delta\eta$  field is consistent with the various observations and physics used to construct, force, and tune the tidal model. Note, however, that a satisfactory comparison is not a guarantee that the model tidal fields are accurate: the possibility exists that nontidal processes affecting the DSI fields somehow compensate for errors in the tidal fields. If the comparison falls short in some significant manner, however, then we need to question the tide models and/or our assumption of time-independent ice shelf flow. With access to multiple tidal models such comparisons allow us to choose the optimum model from those available and estimate the variability of model performance. Since this paper does not aim to determine tides precisely but rather to demonstrate the role of SAR interferometry in tidal description and prediction, we show comparisons only with two models that were readily available to us, the Circum-Antarctic Tidal Simulation (CATS99.4) and FES95.2 [Le Provost et al., 1998], both of which are reviewed below.

Beyond model validation the use of DSI may allow us to investigate whether the observed  $\Delta\eta$  reveals some aspect of sea surface motion that is independent of the tides, for example, a seiche or surge driven by meteorological conditions. Finally, we wish to determine whether the observed  $\Delta\eta$  reveals aspects of the tide

that are difficult to observe and simulate with precision in tidal models. An example of this would be TVWs associated with the diurnal tide whose properties depend on the intricacies of the poorly known topography in the sub-ice shelf cavity and near the ice front.

#### 3.1. Circum-Antarctic Tidal Simulation (CATS99.4)

The CATS99.4 model is an extension of the finite difference, time-stepping model (RPE98.1) described by *Robertson et al.* [1998]. The new model covers the entire globe south of 50°S at a resolution of  $1/4^\circ$  in longitude and  $1/12^\circ$  in latitude ( $\sim 10$  km typical grid node spacing around the Antarctic coast). Eight constituents are modeled, five semidiurnal ( $M_2$ ,  $S_2$ ,  $K_2$ ,  $N_2$ , and  $2N_2$ ) and three diurnal ( $O_1$ ,  $K_1$ , and  $Q_1$ ). Boundary conditions are obtained from the FES95.2 global model described in section 3.2, and local astronomical forcing is included. Tidal periods and frequencies are given in Table 1. The model uses the depth-integrated shallow water equations including terms for quadratic bottom friction and lateral viscosity. The model is fully nonlinear: all constituents are evaluated concurrently and thus can be coupled through the friction parameterizations and advective terms. Maps of the amplitude and phase of the CATS99.4  $M_2$  and  $O_1$  constituents are provided in Plate 3. These two constituents are expected to be the strongest contributors to the DSI, because of their significant energy and favorable periodicity relative to the satellite pass separations.

Several modifications have been made to the RPE98.1 model beyond simply extending the model domain. Open ocean tide height boundary conditions based on the global inverse solution of *Egbert et al.* [1994] and *Egbert* [1997] have been replaced with heights from FES95.2. An error in matching the specifications of land and ice shelves has been fixed, allowing us to use a much smaller lateral viscosity coefficient (now  $10 \text{ m}^2 \text{ s}^{-1}$  instead of  $1000 \text{ m}^2 \text{ s}^{-1}$  in RPE98.1). New bathymetric data in the southwestern Weddell Sea collected

**Table 1.** Period of the Eight Principal, Explicitly Modeled Tidal Constituents Used in the FES95.2 and CATS99.4 Tidal Models, in Order of Decreasing Period

Constituent	Period, hours
$Q_1$	26.87
$O_1$	25.82
$K_1$	23.93
$2N_2$	12.91
$N_2$	12.66
$M_2$	12.42
$S_2$	12.00
$K_2$	11.97



during the Ronne Polynya Experiment (ROPEX) cruise in early 1998 [Nicholls *et al.*, 1998; Padman *et al.*, 2000] have been used to revise the model depth grid. The effect of this bathymetry revision is greatest along the southern continental shelf break but also has some influence along the Ronne ice front and elsewhere in the Weddell Sea [Padman *et al.*, 1998].

The CATS99.4 model includes three large “ice islands” north of Berkner Island (see Figure 1). The ice islands are tabular icebergs that calved off the Filchner Ice Shelf in 1986 and subsequently grounded on the shallow Berkner Bank [Nøst and Østerhus, 1998]. These ice islands were still present in 1996 during the period that the SAR data used in this study were obtained. The effect of adding these ice islands is significant: comparison with an earlier version of the CATS model (CATS99.2) [Padman and Kottmeier, 2000] that did not include the islands demonstrated that the tidal regime along the Filchner ice front is significantly altered when the islands are added.

### 3.2. Grenoble Global Tidal Model (FES95.2)

The FES95.2 model [Le Provost *et al.*, 1998] was developed from the pure hydrodynamic solution model FES94.1 [Le Provost *et al.*, 1994]. FES94.1 was built to predict the tidal contribution to sea surface height variations seen by the T/P altimeter. The model is global, including the entire Arctic Ocean, the under-ice shelf areas of the Weddell and Ross Seas, and most shallow seas. Eight constituents have been simulated;  $M_2$ ,  $S_2$ ,  $N_2$ ,  $K_2$ ,  $2N_2$ ,  $K_1$ ,  $O_1$ , and  $Q_1$ . Eighteen minor constituents have been deduced by admittance from these eight major ones. The resolution of the numerical model varies spatially, with a finite element grid that is refined over shelves and along the coasts. The minimum cell dimension is 10 km [see Le Provost *et al.*, 1994, Figure 1]. This high resolution concentrated over the major topographic features of the world ocean allows the finite element model to catch the local characteristics of the tidal waves that would be unresolved in the classical coarser hydrodynamical ocean tide models.

The FES95.2 model improves on the predictive capability of FES94.1 by assimilating into the hydrodynamic model the empirical University of Texas Center for Space Research (CSR) tidal solution (CSR2.0) using the representer method developed by Egbert *et al.* [1994]. The CSR2.0 solutions were computed at the end of 1994 from 2 years of T/P data. The data set used in the assimilation is a sample of CSR2.0 on a  $5^\circ \times 5^\circ$  grid for ocean depths  $> 1000$  m. The assimilation has been performed for the Atlantic, Indian, and Pacific Oceans. The standard release of the FES95.2 solutions is a  $0.5^\circ \times 0.5^\circ$  gridded version of the full resolution solution computed on the finite element grid. The software provided with this release interpolates to user-specified positions within this regular grid.

### 3.3. Ocean Tidal Model Comparison With SAR Differential Interferometry

Comparison between the model prediction and the DSI-derived sea surface displacement changes,  $\Delta\eta_M$  and  $\Delta\eta$ , respectively, required synthesis of the instantaneous model sea surface height fields at the times of the four satellite passes used to construct each DSI. These syntheses were made using the amplitude and phase representations of  $K$  tidal constituents constructed from model output. For both models,  $K = 26$ , consisting of eight constituents that are explicitly determined and eighteen that are estimated by admittance. Appendix A describes the relationship between the amplitude and phase of tidal constituents and the observed  $\Delta\eta$ . The modeled  $\Delta\eta_M$  is constructed in a similar fashion.

Satellite pass times  $t_1$  and  $t_2$ , as well as  $t_3$  and  $t_4$ , were separated by exactly 24.0 hours. The  $\eta_M(t_1)$  and  $\eta_M(t_2)$  fields, as well as the  $\eta_M(t_3)$  and  $\eta_M(t_4)$  fields, thus appeared to be quite similar because the periods of all the diurnal and semidiurnal tidal constituents are close to 12 or 24 hours. Nevertheless, the small differences in the fields at the four pass times are the cause of the signal in the DSIs, and the fields resulting from the double-differencing operation are extremely sensitive to small errors in the tidal predictions. The method is a much more rigorous test of the models than the simpler comparisons of time series of tidal data would be [see, e.g., Robertson *et al.*, 1998; Padman and Kottmeier, 2000]. Our studies also revealed the importance of including minor tidal constituents by admittance. Without admittance, i.e., by creating tidal predictions by summation of just the eight explicitly modeled constituents, the  $\Delta\eta_M$  fields were much less consistent with the measured DSIs.

**3.3.1. Model/observation comparison: Ronne Ice Shelf.** The  $\Delta\eta_{\text{FES95.2}}$  and  $\Delta\eta_{\text{CATS99.4}}$  are compared with the interferogram-derived  $\Delta\eta$  in Plate 4 and Figure 2. The agreement is generally good. Averaged over the ice shelf, the mean of  $\Delta\eta_{\text{FES95.2}}$  is  $\sim 3$  cm less than the mean  $\Delta\eta$  estimated from SAR, while the standard deviation of the error is  $\sim 7$  cm. The offset is larger for CATS99.4 but with a similar standard deviation. The error standard deviations of both models are comparable to the rms error reported by Egbert [1997] for global model comparisons with T/P altimetry (the constraining data used in developing the two assimilation-based tidal models). We have compared the CATS99.4 model with recently recovered current meter data along the Ronne ice front [Woodgate *et al.*, 1998], and the model performs very well in this region. The general agreement between DSI and the models is therefore not surprising.

Although this model agreement with data is encouraging, it is clear from Plate 4 and Figure 2 that the DSI contains information that is not accurately predicted by the tide models. The principal gradient in the  $\Delta\eta$  fields

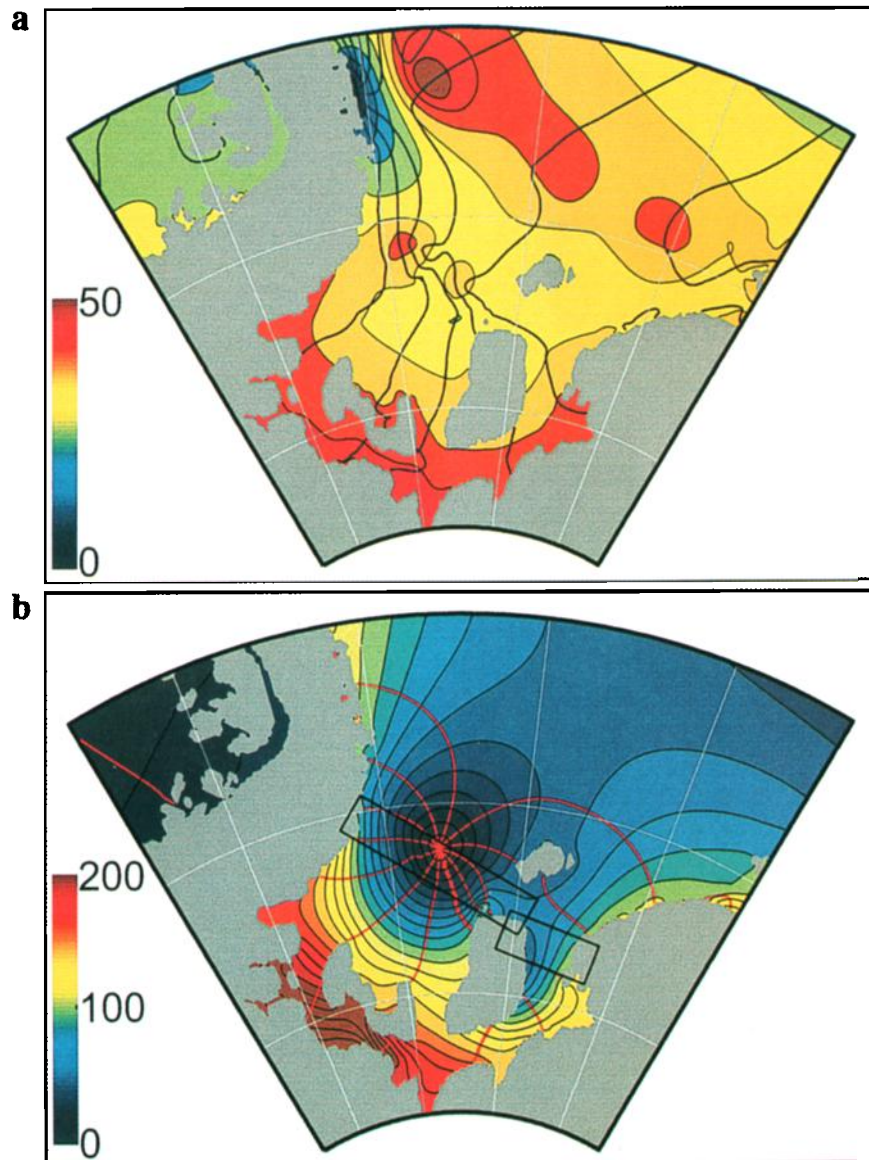


**Plate 3.** The amplitude (color shading and black contours) and phase (blue contours) for (a)  $O_1$  and (b)  $M_2$  from the CATS99.4 tidal model (see section 3.1). For  $O_1$ , contour intervals are 5 cm for amplitude and  $10^\circ$  for phase. For  $M_2$ , contour intervals are 10 cm and  $30^\circ$ . Rectangles denote approximate locations of differential SAR interferograms (DSIs) presented in Plates 1 and 2. The direction of phase propagation is generally from east to west for  $O_1$ , and clockwise around the amphidromic point for  $M_2$ . The  $M_2$  amphidromic point is located near the center of the ice front on the Ronne Ice Shelf. The location of the FES95.2  $M_2$  amphidromic point is  $\sim 25$  km to the south of that shown here for CATS99.4.

for the Ronne Ice Shelf is parallel to the ice front and is due primarily to the  $M_2$  tidal constituent, which has an amphidromic point on the ice front near  $54^\circ$  W (see Plate 3). This gradient has been well modeled, giving rise to the good overall correlation between the model and data estimates of  $\Delta\eta$ . However, the models, in particular CATS99.4, underestimate the magnitude of the bump-and-dimple structure in the  $\Delta\eta$  field near the center of the SAR data scene. There are at least two possible explanations for this observation. First, the models may be unable to predict accurately tidal TVWs,

which occur predominantly in the diurnal band, have small length scales, and are sensitive to variations in both water depth and spatial gradients of water depth [Middleton *et al.*, 1987; Padman and Kottmeier, 2000]. Second, recall that the bump-and-dimple structure lies quite close to the  $M_2$  amphidromic point. From the 10 km resolution output from CATS99.4 we find that the gradient of  $M_2$  sea surface elevation amplitude at the amphidrome is  $\sim 0.25$  cm km $^{-1}$ . Thus an error of 20 km in the model location of the amphidrome could cause a 5 cm error in the height field (although not necessarily

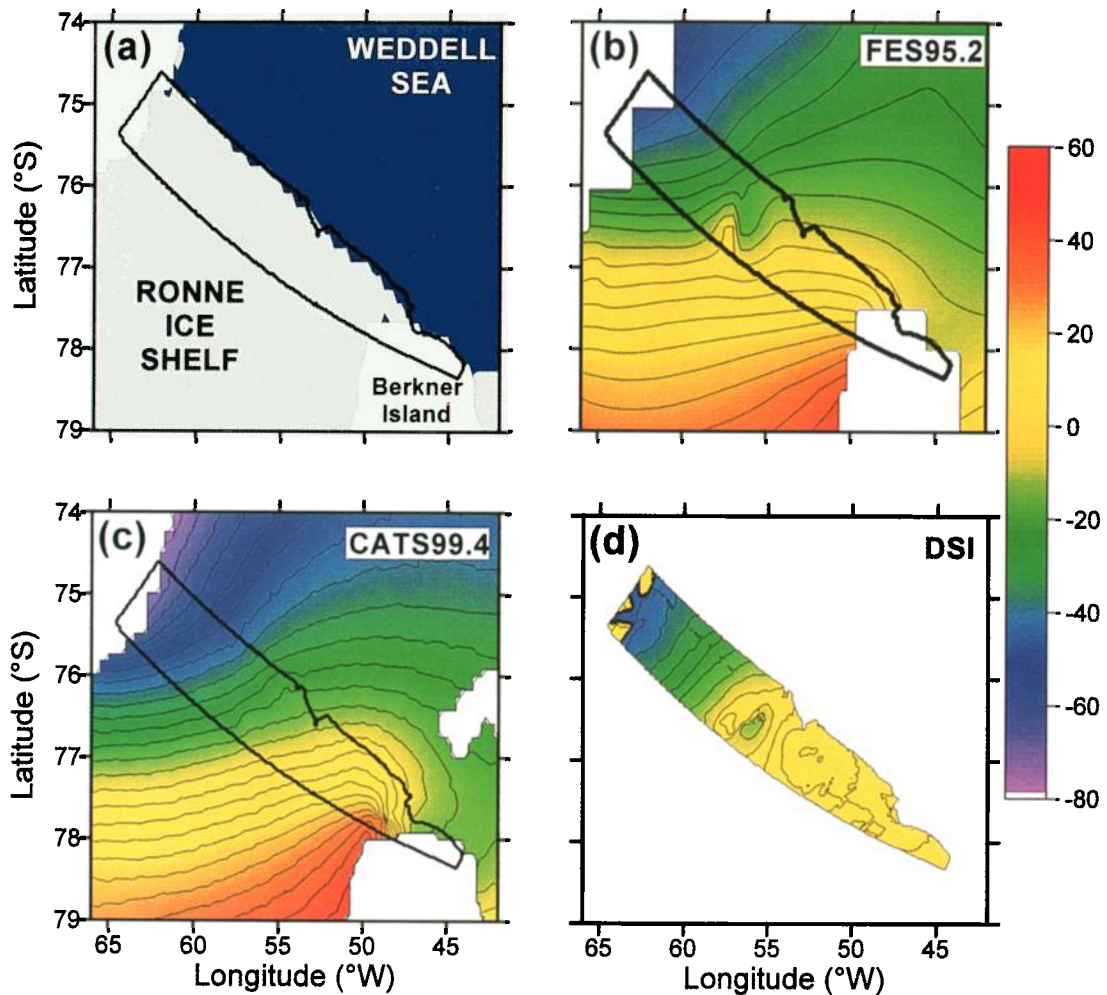


**Plate 4.** Comparison between (b)  $\Delta\eta_{\text{FES95.2}}$ , (c)  $\Delta\eta_{\text{CATS99.4}}$ , and (d)  $\Delta\eta$  for the Ronne Ice Shelf. The color map ranges from -80 to 60 cm, and the line contour interval is 5 cm. The solid outlined region describes the locations of good data in the DSI.

in the derived  $\Delta\eta_M$ ). This is not a large spatial error in models with minimum grid spacings of order 10 km, and we note that the  $M_2$  amphidromes in the FES95.2 and CATS99.4 models are separated by  $\sim 25$  km. These errors can be ascribed to the poor quality of bathymetric and water column thickness data in the southern Weddell Sea including under the FRIS. We shall return to these issues briefly in section 4.

Nontidal sources for the bump-and-dimple structure need to be considered as well. For example, an ocean eddy with a sea surface height expression passing quickly through the region could explain the feature. We note, however, that the FES95.2 model shows some signs of the bump-and-dimple structure, leading us to believe that the origin of the feature is tidal and that the model/data mismatch represents errors due to the inherent physical simplifications of the models and the influence of poor bathymetric data.

**3.3.2. Model/observation comparison: Filchner Ice Shelf.** The model-derived values of  $\Delta\eta_{\text{FES95.2}}$  and  $\Delta\eta_{\text{CATS99.4}}$  for the Filchner Ice Shelf DSI are shown

in Plate 5. The model-derived values are compared with the interferogram-derived  $\Delta\eta$  in Figure 2 and Plate 5. The FES95.2 model is less successful at predicting  $\Delta\eta$  for the Filchner than for the Ronne Ice Shelf. There is an offset of  $\sim 20$  cm between the DSI and FES95.2. The mean offset between CATS99.4 and the DSI, however, is  $< 3$  cm, while the square root of the mean square error is  $< 4$  cm (Figure 2 and Plate 5).

On the basis of comparisons between the Filchner DSI and an earlier version of the CATS model (CATS99.2) [Padman and Kottmeier, 2000] we believe that much of the improved performance of CATS99.4 relative to FES95.2 is due to our inclusion of the ice islands north of Berkner Island (see section 3.1). For CATS99.2, which lacks the ice islands, the mean offset between modeled  $\Delta\eta_{\text{CATS99.2}}$  and  $\Delta\eta$  was  $\sim 12$  cm, less than for FES95.2 but significantly worse than for CATS99.4.

## 4. Discussion

The comparisons presented in section 3 suggest that most of the signal seen in DSIs for the FRIS is due to tides. While the agreement between tidal models and

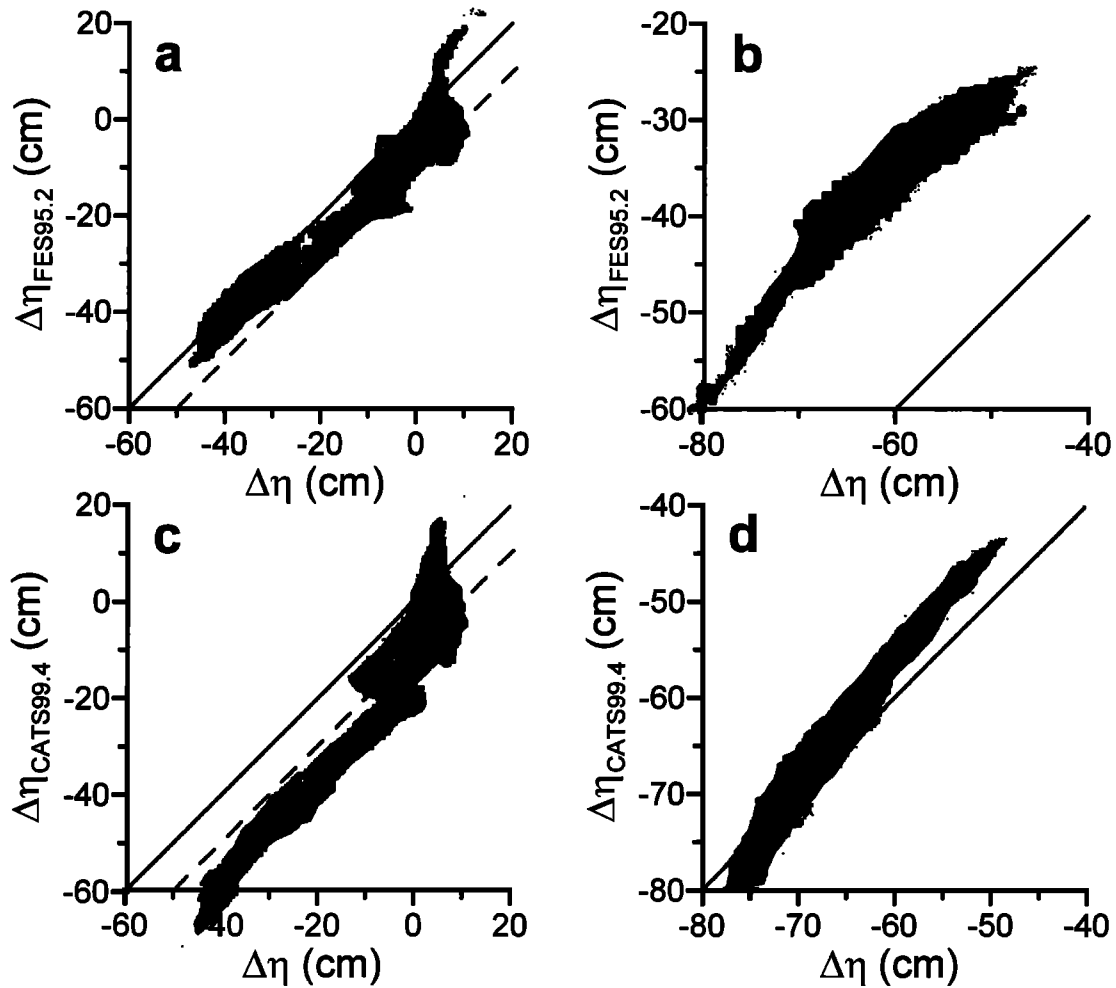


**Figure 2.** Comparison between model predictions  $\Delta\eta_M$  and the observations  $\Delta\eta$  (all units are in centimeters): (a) and (b) the FES95.2 model and (c) and (d) the CATS99.4 model. Figures 2a and 2b refer to the Ronne DSI, and Figures 2b and 2d refer to the Filchner DSI. Shaded diagonal lines indicate model equivalence with data. Dashed shaded lines indicate model equivalence when the inverse barometric effect of  $\sim 10$  cm (see Table 2) is taken into account.

measured  $\Delta\eta$  is very encouraging, weaknesses still exist. The CATS99.4 model does not capture the bump-and-dimple feature on the Ronne ice front, while FES95.2 performs poorly along the Filchner ice front. On the basis of the present and related studies we identify three principal sources of mismatch between modeled and measured  $\Delta\eta$ . These are errors in model grids of water column thickness, the use of a finite set of tidal constituents in model prediction of  $\Delta\eta$ , and nontidal ocean height variability. We address each of these topics below.

#### 4.1. Errors in Model Grids of Water Column Thickness

In previous studies we have found that tidal currents along the continental shelf break in the southern Weddell Sea were very sensitive to the model bathymetry grid [Padman *et al.*, 1998]. This study compared tidal currents using bathymetry grids developed before and

after the ROPEX cruise [Nicholls *et al.*, 1998; Padman *et al.*, 2000] to the southwestern Weddell Sea. In particular, changing the model bathymetry for the General Belgrano Bank (centered near  $73^\circ\text{S}$ ,  $49^\circ\text{W}$ ) from the shallower pre-ROPEX value to the more realistic updated value was found to have a profound effect on diurnal band tidal energy along the entire southern continental slope. The effect of these changes to the depth grid are less obvious in sea surface height but still significant for the comparisons discussed herein.

We propose that a similar influence of bathymetry is responsible for some of the mismatch between modeled and measured values of  $\Delta\eta$  along the ice front of the FRIS (see section 3.3). We believe that the bump-and-dimple feature in the Ronne ice front DSI is caused either by the presence of TVWs that are not well resolved by the tide models or by a small model error in locating the  $M_2$  amphidrome. Both of these potential errors are expected to be strongly dependent on bathymetric qual-



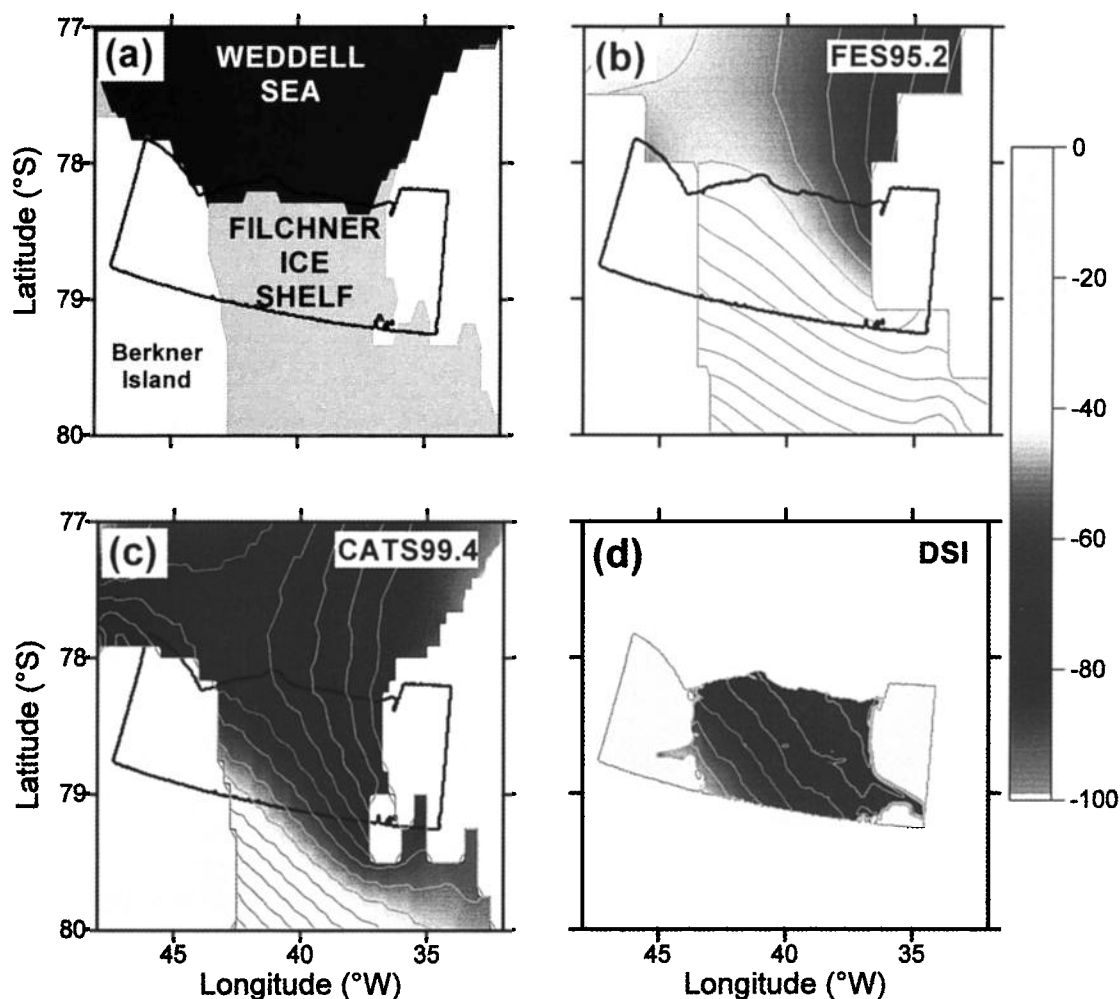


Plate 5. Comparison between (b)  $\Delta\eta_{\text{FES95.2}}$ , (c)  $\Delta\eta_{\text{CATS99.4}}$ , and (d)  $\Delta\eta$  for the Filchner Ice Shelf. The color map ranges from -100 to 20 cm, and the line contour interval is 5 cm. The solid outlined region describes the location of good data in the DSI.

ity, specifically including water column thickness errors under the FRIS. We note that the CATS99.4 model performs very well to the east of the  $M_2$  amphidrome (especially after correcting for the inverse barometer effect (IBE) (see Figure 2c)) but less well to the west. This observation is consistent with the errors being caused primarily while the tidal energy flux is under the ice shelf: east of the amphidrome, the  $M_2$  energy flux is southward into the under-ice cavity [see also Robertson *et al.*, 1998, Plate 4a], while  $M_2$  tidal energy on the western end of the Ronne ice front has circulated under the FRIS.

We also found that for the Filchner DSI the predictive skill of the CATS series of models improved significantly when the ice islands on Berkner Bank were added. The mean error for the version without the ice islands (CATS99.2) [see Padman and Kottmeier, 2000] was  $\sim 12$  cm, which was reduced to  $< 3$  cm when the ice islands were included (CATS99.4, the model used herein).

#### 4.2. Excluded Tidal Constituents

We tested the predictive skill of CATS99.4 with and without the inclusion of the 18 minor tidal constituents that are estimated by admittance [see Le Provost *et al.* 1998, Table 2]. That is, model predictions were made first using only the eight explicitly modeled constituents ( $M_2$ ,  $S_2$ ,  $K_2$ ,  $N_2$ ,  $2N_2$ ,  $O_1$ ,  $K_1$ , and  $Q_1$ ) and then adding the 18 additional constituents and rerunning the comparisons. We found that the additional constituents were crucial to model predictive skill. This observation initially surprised us since most of the total tidal potential energy is captured with the eight major constituents. However, the construction of a modeled DSI involves double differencing of tidal height estimates, so that many of the major constituents become insignificant in the DSI ( $S_2$  does not contribute at all, while  $K_1$  and  $K_2$  are only poorly resolved by the 1.0 day separation of the ERS-1 and ERS-2 passes).

The 18 minor constituents are all in the diurnal or semidiurnal frequency bands. Additional, possibly sig-

nificant, energy may be present in long-period tides as well. These tides will need to be explicitly modeled before concluding that nontidal sources of ocean height variability must be responsible for the mismatch between the modeled and measured DSIs.

#### 4.3. Nontidal Ocean Height Variability

Ocean height can vary because of nontidal processes such as storm surges, ocean eddies, and the IBE. Here we discuss just the potential influence of the IBE since it is easy to estimate from available data and will be shown to be of sufficient magnitude to explain much of the existing mismatch between models and measured  $\Delta\eta$ .

The IBE involves the ocean's isostatic response to changes in atmospheric pressure ( $P_{\text{atm}}$ ) [Gill, 1982, p. 337]. The approximate ocean surface response for the IBE is  $\sim 1 \text{ cm (mbar } P_{\text{atm}})^{-1}$ , thus a 50 mbar increase in  $P_{\text{atm}}$  causes about a 50 cm decrease in  $\eta$ . Air pressure tends to vary with time scales of a few days; thus much of the variability in the IBE is lost when a DSI is calculated on the basis of two interferograms with 1 day pass separations. However, the remaining signal may be comparable in magnitude to the tide model predictive skill. To estimate the influence of the IBE on our model/data comparisons, we reviewed surface air pressure records from two stations that were active during 1996, Halley Base (75.5°S, 26.6°W, east of the Filchner Ice Shelf) and Butler Island (72.2°S, 60.3°W, west of the Ronne Ice Shelf). Each record consists of  $P_{\text{atm}}$  recorded every 3 hours. The predicted contribution of the IBE to the DSI can then be estimated from  $\Delta\eta_{\text{IBE}} = (\eta_{\text{IBE},4} - \eta_{\text{IBE},3}) - (\eta_{\text{IBE},2} - \eta_{\text{IBE},1})$ , where  $\eta_{\text{IBE},j}$ ,  $j = 1, \dots, 4$ , is the sea surface displacement due to the IBE at the time of the  $j$ th SAR image used in constructing the DSI.

The predicted values of  $\Delta\eta_{\text{IBE}}$  for each station and for the two particular time sets  $t_n$  corresponding to the actual Ronne and Filchner DSIs discussed here are shown in Table 2. In Table 2, positive values of the IBE influence in the DSI imply that in the absence of tides and other contributors to the DSI,  $\Delta\eta$  would also be positive. When the IBE is included in the tidal prediction for the Ronne Ice Shelf, the match between  $\Delta\eta_{\text{FES95.2}}$

and  $\Delta\eta$  remains of similar magnitude but changes sign, while the agreement with  $\Delta\eta_{\text{CATS99.4}}$  improves (see Figure 2). We cannot justify an IBE correction for the Filchner Ice Shelf DSI since the nearest station, Halley Bay, shows only a 1 cm IBE contribution to the DSI.

The magnitudes of the IBE correction for the time sets for the two DSIs discussed here vary from negligible (1 cm) to  $\sim 10$  cm. We can also use the records of  $P_{\text{atm}}$  at the two coastal stations to determine the statistical properties of  $\Delta\eta_{\text{IBE}}$ . In this case we estimate all values of  $\Delta\eta_{\text{IBE}}$  for sets of four satellite passes that retain the same time separations as in the real DSIs ( $(t_j - t_1), j = 2, \dots, 4$ ) but with  $t_1$  taken at the times of each of the 3 hourly records of  $P_{\text{atm}}$ . As required from the method used to estimate  $\Delta\eta_{\text{IBE}}$ , the mean of  $\Delta\eta_{\text{IBE}}$  at both stations is very close to zero. The largest values of  $\Delta\eta_{\text{IBE}}$  are  $\sim 20$  cm, and the standard deviation for each station is  $\sim 8$  cm. That is, signals of order 10 cm due to the IBE contribution to sea surface height are predicted to occur in a DSI based on the pass separations for the ERS-1 and ERS-2 tandem mission.

Note that the spatial scales of the IBE correction will mimic the scales of variability in  $P_{\text{atm}}$ , and so, for the size of the regions covered by the present DSIs we expect the IBE correction will be roughly constant across the DSI. It is, however, plausible that part of the spatial variability of the error between  $\Delta\eta_{\text{M}}$  and  $\Delta\eta$  can be explained by spatial variability in  $\Delta\eta_{\text{IBE}}$ .

## 5. Summary

Differential SAR interferometry (DSI) can be used to validate tidal models under floating ice shelves. When combined with the use of DSI in determining the location and movement of ice shelf grounding lines [e.g., Rignot, 1996, 1998a,b], DSI is seen to be a powerful tool for monitoring floating ice shelves and the oceanic processes that affect their stability. Even with the small DSI data set described herein, we have shown that these data identify deficiencies in existing tidal model performance. In the present case, that of tides in the southern Weddell Sea, DSI has provided us with data over a large region in which few conventional tidal data points exist.

These analyses have illustrated to us the need to improve our models of topographic vorticity waves (TVWs) at diurnal frequencies along the front of the Ronne Ice Shelf and to include corrections for the inverse barometer effect (IBE). The TVWs are energetic over only a small fraction of the Weddell Sea; however, they occur in regions that are critical to the large-scale thermohaline structure of the region. The TVWs may play a critical role in sea ice divergence along the continental shelf break and along the Ronne ice front [Padman and Kottmeier, 2000]. They may also enhance mixing across the strong topographic vorticity gradient at the ice front, providing a method for ventilation of the under-ice cavity that is not present in models with negligible mixing. (In these models, advective exchange

**Table 2.** Sea Surface Displacement Change Due to the Inverse Barometer Effect Predicted for the Ronne and Filchner DSIs Using Surface Air Pressure Recorded at 3 Hour Intervals at Halley Bay and Butler Island

	$\Delta\eta_{\text{IBE}}$ , cm	
	Halley Bay	Butler Island
Ronne	+12	+9
Filchner	-1	+5

A positive value implies a positive contribution to  $\Delta\eta$ .

across the ice front is minimal because of the strong topographic vorticity constraint.) The IBE is expected to contribute up to 50 cm variability in ice shelf elevation ( $\sim 1 \text{ cm (mbar } P_{\text{atm}})^{-1}$ ) and will also vary spatially as  $P_{\text{atm}}(x, y)$  varies under passing weather systems.

We have also demonstrated that DSI could be used to resolve tidal constituents under ice shelves (Appendix B) directly, although this is not feasible with existing SAR data. The motion of the mobile sea ice also contains a strong tidal signal [Padman and Kottmeier, 2000], and SAR sensors could be valuable tools for determining this motion through feature tracking of individual ice floes [Drinkwater, 1998]. In each case, however, optimum orbit selection is critical to the usefulness of the resultant data for defining the tidal contribution. An example of the planning process for orbit configuration is provided by Parke *et al.* [1987] for the T/P altimeter mission. In this case the primary planning goal in relation to tides was to ensure that the most energetic constituents were not aliased in the T/P 10 day repeat mission (actual repeat interval of 9.9156 days) into low frequencies that might contain significant ocean variability, such as the annual cycle and Rossby waves, and that the aliased frequencies for each constituent were unique. The resultant T/P orbit achieved these goals for most major tidal constituents [Schlax and Chelton, 1994; Schrama and Ray, 1994] (see also other papers in the TOPEX/Poseidon special issue of the *Journal of Geophysical Research*, Volume 99(C12), 24,369-25,062, 1994). Similar requirements exist for SAR missions to study ice shelf tides, namely, that no major tides are “frozen” (i.e., have exactly the same phase at the time of each satellite pass), the aliased tidal signals for different constituents are separable during a mission duration of 1-3 years, and the aliased tidal energy will not be confused with other potentially energetic signals (e.g., the annual cycle). Furthermore, in “tandem” missions such as the ERS-1/ERS-2 combined mission period described here, the time separation of the independent satellites also needs to be considered. These conditions are not easily met, and in practice, the interpretation of satellite-based geophysical data containing tides, for satellite systems with repeat intervals much greater than 1 day, will continue to rely on the use of the data either to drive the improvement of purely dynamical models as described here or in formal data assimilation schemes [see, e.g., Egbert *et al.*, 1994; Egbert, 1997]. Nevertheless, careful selection of orbit configuration can significantly improve the value of SAR data for constraining and improving tidal models by these techniques for both the ice shelves and the open ocean.

## Appendix A: Relationship Between Tide and SAR Data

Assuming the sea surface elevation (SSE) is due only to ocean tides, the DSI-derived  $\Delta\eta$  given by (2) is related to the instantaneous sea surface heights  $\eta(t_j, \lambda, \phi)$ ,

which are given by

$$\eta(t_j, \lambda, \phi) = \sum_{k=1}^K \Re [Z_k(\lambda, \phi) e^{i\omega_k t_j}]. \quad (\text{A1})$$

In (A1),  $t_j, j = 1, \dots, 4$ , are the times of each of the four satellite passes,  $\lambda$  and  $\phi$  are the longitude and latitude, respectively,  $K$  is the number of tidal constituents used in the superposition,  $Z_k(\lambda, \phi)$  is a complex-valued function that specifies the amplitude and phase of sea surface elevation associated with the  $k$ th tidal constituent,  $\omega_k$  is the real-valued frequency of the  $k$ th constituent in  $\text{rad s}^{-1}$ , and the operator  $\Re(\cdot)$  extracts the real part of its argument. The SSE difference determined by DSI can thus be expressed by

$$\Delta\eta(\lambda, \phi) = \sum_{k=1}^K \Re [c_k Z_k(\lambda, \phi)], \quad (\text{A2})$$

where the complex-valued coefficients  $c_k$  are

$$c_k = (e^{i\omega_k t_1} - e^{i\omega_k t_2} - e^{i\omega_k t_3} + e^{i\omega_k t_4}) \quad (\text{A3})$$

or

$$c_k = e^{i\omega_k t_1} (1 - e^{i\omega_k (t_2 - t_1)} - e^{i\omega_k (t_3 - t_1)} + e^{i\omega_k (t_4 - t_1)}). \quad (\text{A4})$$

For the orbit periodicity of the ERS-1 and ERS-2 passes used in this study,

$$c_k = e^{i\omega_k t_1} (1 - e^{i\omega_k 1} - e^{i\omega_k 35} + e^{i\omega_k 36}), \quad (\text{A5})$$

where the numbers 1, 35, and 36 denote time difference in days. (In (A5),  $\omega_k$  must be specified in  $\text{rad d}^{-1}$ .)

Inspection of (A5) reveals that the amplitudes of the  $c_k, k = 1, \dots, K$ , depend only on the satellite orbit periodicity relative to the periods  $2\pi/\omega_k$  of the tidal constituents; that is, the  $c_k$  values depend only on the time separation of passes  $(t_2 - t_1)$ ,  $(t_3 - t_1)$ , and  $(t_4 - t_1)$ . These time separations are integral numbers of days and are thus exact multiples of the 12.0000 hour period of the  $S_2$  tide. This means that the  $S_2$  tide cannot contribute to the  $\Delta\eta$  values observed in our study. Similarly, the contributions of the  $K_1$  and  $K_2$  tides are also small (see Table 1). The  $Q_1$ ,  $2N_2$ , and  $N_2$  tides, while having favorable periods for contributing to  $\Delta\eta$ , are relatively weak in the Weddell Sea, having amplitudes always less than several centimeters. This leaves  $M_2$  and  $O_1$  as the primary contributors to  $\Delta\eta$  because they have both favorable periodicity and strong amplitude in the Weddell Sea. Maps of the amplitude and phase of  $M_2$  and  $O_1$  derived from the CATS99.4 ocean tide model (section 3.1) are shown in Plate 3.

## Appendix B: Theory of Inversion of DSI Data for Tidal Parameters

The linear relationship between  $\Delta\eta$  and the  $K$  tidal constituent functions  $Z_k$  with  $k = 1, \dots, K$  in (A2) sug-

gests that a set of simultaneous linear equations may be formulated to determine uniquely the various  $Z_k$  values from an appropriate number of DSI-determined  $\Delta\eta$  values. We develop this suggestion for future reference, even though it is impractical with existing data sets and is not used in this study.

Given  $M$  DSIs of a single region constructed from  $4M$  satellite passes at times  $t_j^{[m]}$ ,  $j = 1, \dots, 4$ , where  $m = 1, \dots, M$ , is a sequence of  $M$   $\Delta\eta$  fields, denoted  $\Delta\eta^{[m]}$ ,  $m = 1, \dots, M$ , are available for analysis. Following the notation defined in (A4), a sequence of coefficients  $c_k^{[m]}$ ,  $k = 1, \dots, K$  and  $m = 1, \dots, M$ , can be computed from  $t_j^{[m]}$ . Expressing the real and imaginary parts of the tidal constituent functions as

$$Z_k(\lambda, \phi) = x_k(\lambda, \phi) + iy_k(\lambda, \phi) \quad (\text{B1})$$

and denoting the real and imaginary parts of the  $c_k^{[m]}$  as

$$c_k^{[m]} = \delta_k^{[m]} + i\epsilon_k^{[m]}, \quad (\text{B2})$$

the set of simultaneous linear equations determining the  $Z_k$  values from the  $\Delta\eta^{[m]}$  values may be expressed as follows:

$$\mathbf{C} \mathbf{Z} = [\mathbf{C11} \quad \mathbf{C12}] \mathbf{Z} = \mathbf{H}, \quad (\text{B3})$$

where

$$\mathbf{Z}^T = [x_1 \ x_2 \ \dots \ x_K \ y_1 \ y_2 \ \dots \ y_K], \quad (\text{B4})$$

$$\mathbf{H}^T = [\Delta\eta^{[1]} \ \Delta\eta^{[2]} \ \dots \ \Delta\eta^{[M]}]. \quad (\text{B5})$$

The submatrices of  $\mathbf{C}$ ,  $\mathbf{C11}$  and  $\mathbf{C12}$ , are each  $M \times K$  matrices with coefficients

$$C11_{km} = \delta_k^{[m]}, \quad (\text{B6})$$

$$C12_{km} = -\epsilon_k^{[m]}. \quad (\text{B7})$$

If  $M \geq 2K$  (with the strict inequality desirable to reduce noise) and satellite orbit periods are not exact multiples of any of the tidal constituent periods, the matrix  $\mathbf{C}$  can have full rank, and (B3) may be inverted for the  $Z_k$  functions using an appropriate inverse technique (e.g., least squares).

In the present study the  $\mathbf{C}$  matrix constructed by the above means is not invertible because  $M = 1$  and several constituents contribute significant energy to the total DSI signal. Recall from section 4.2 that while the two tidal models that we considered only explicitly modeled 8 constituents, the additional 18 constituents obtained by admittance were required to obtain a satisfactory match between the tidal models and DSI fields. Thus the approximate number of necessary DSIs for a successful data inversion is  $2K = 52$ , even assuming that  $\Delta\eta$  is purely tidal. In practice, as we showed in section 4, nontidal ocean variability such as the IBE can also contribute significant energy to the time series of  $\eta$ , further increasing the number of DSIs needed to

obtain accurate tidal constituent amplitude and phase estimates. Even under the best of circumstances, however, inversion of the  $\mathbf{C}$  matrix may not be practical or even possible. This is because some of the  $c_k$  coefficients used to construct  $\mathbf{C}$  may be zero when the time separations of satellite orbits are exact or near multiples of tidal periods, as in the ERS-1/ERS-2 tandem mission described herein.

Although data from ERS-1 and ERS-2 are unfavorable for the direct determination of sub-ice shelf tides, the comparisons of the two DSI examples studied here with the results of tide models illustrate the future potential of DSI for tidal analysis. Efforts are currently underway, for instance, to launch a lightweight SAR (referred to as NASA's "LightSAR") sometime in year 2002 or earlier. The desired repeat pass cycle of LightSAR would be of  $\sim 10$  days, in a Sun-synchronous mode. The radar frequency will be L band, which gives a 24 cm wavelength. This wavelength is 5 times that of the radar used by ERS-1 and ERS-2. Hence, for a 10 day repeat orbit the fringe rate will be approximately equal to that obtainable with ERS-1 and ERS-2 separated by 2 days. The mission life of LightSAR is expected to be 5 years, which would give sufficient coverage of the ice shelves to accomplish tidal analysis by the method described here.

**Acknowledgments.** Work performed at Jet Propulsion Laboratory, California Institute of Technology, was supported by a contract with the National Aeronautics and Space Administration (NASA). Support for the University of Chicago component of this project was provided by NASA (NAGW-5-4087) and the National Science Foundation Office of Polar Programs (OPP-9818622). The satellite data needed for this research were provided by the European Space Agency (ERS-1/2 project code: AO2.USA.160). The ocean tidal modeling at Oregon State University (OSU) and Earth & Space Research (ESR) was supported by grants from the National Science Foundation Office of Polar Programs (OPP-9615525 and OPP-9896041) and from NASA (NAG5-7790). We thank Charlie Werner for providing a SAR processor to generate the SAR interferograms, Andrew Gabriel for help in the project inception, and David Vaughan, Chris Doake, Richard Frolich, Richard Hindmarsh, and other colleagues at the British Antarctic Survey for providing ice thickness data for the FRIS and for their many suggestions during the course of the research reported here. Jonathan Bamber provided a digital topographic map of Antarctica. Landsat MSS data (georeferenced by the Institut für Angewandte Geodäsie (IfAG), Frankfurt am Main) proved to be invaluable in the verification and refinement of SAR data georeferencing and were provided courtesy of H. Bennat and J. Sievers. Gary Egbert and Lana Erofeeva at OSU provided advice and computer resources for running the tidal model. Christian Le Provost provided the tidal prediction package for the FES95.2 tidal model, and Susan Howard at ESR was responsible for running this package for us. We thank Philippe Techine for providing details of the FES95.2 bathymetry for the southern Weddell Sea. We thank Christian Le Provost and Keith Nicholls for insightful criticisms leading to constructive revisions of the manuscript, including the suggestion to include the Berkner Bank ice islands in CATS99.4.



## References

- Bamber, J. L., and R. A. Bindschadler, An improved elevation dataset for climate and ice-sheet modelling: Validation with satellite imagery, *Ann. Glaciol.*, **25**, 439-444, 1997.
- Drinkwater, M. R., Satellite microwave radar observations of Antarctic sea ice, in *Analysis of SAR Data of the Polar Oceans*, pp. 145-187, edited by C. Tsatsoulis and R. Kwok, Springer-Verlag, New York, 1998.
- Egbert, G. D., Tidal data inversion: Interpolation and inference, *Prog. Oceanogr.*, **40**, 53-80, 1997.
- Egbert, G. D., A. F. Bennett, and M. G. G. Foreman, TOPEX/Poseidon tides estimated using a global inverse model, *J. Geophys. Res.*, **99**, 24,821-24,852, 1994.
- Foldvik, A., J. H. Middleton, and T. D. Foster, The tides of the southern Weddell Sea, *Deep Sea Res., Part A*, **37**, 1345-1362, 1990.
- Frolich, R. M., and C. S. M. Doake, Synthetic aperture radar interferometry over Rutford Ice Stream and Carlson Inlet, Antarctica, *J. Glaciol.*, **44**, 77-92, 1998.
- Gabriel, A. K., R. M. Goldstein, and H. A. Zebker, Mapping small elevation changes over large areas: Differential radar interferometry, *J. Geophys. Res.*, **94**, 9183-9191, 1989.
- Gill, A. E., *Atmosphere-Ocean Dynamics, Int. Geophys. Ser.*, vol. 30, 662 pp., Academic, San Diego, Calif., 1982.
- Goldstein, R. M., H. Engelhardt, B. Kamb, and R. M. Frolich, Satellite radar interferometry for monitoring ice sheet motion: Application to an Antarctic ice stream, *Science*, **262**, 1525-1530, 1993.
- Hartl, P., K. H. Thiel, X. Wu, C. Doake, and J. Sievers, Application of SAR interferometry with ERS-1 in the Antarctic, *Earth Obs. Q.*, **43**, 1-4, 1994.
- Holdsworth, G., Tidal interaction with ice shelves, *Ann. Geophys.*, **33**, 133-146, 1977.
- Le Provost, C., M. L. Genco, F. Lyard, P. Vincent, and P. Canceil, Tidal spectroscopy of the world ocean tides from a finite element hydrodynamic model, *J. Geophys. Res.*, **99**, 24,777-24,798, 1994.
- Le Provost, C., F. Lyard, J. M. Molines, M. L. Genco, and F. Rabilloud, A hydrodynamic ocean tide model improved by assimilating a satellite altimeter-derived data set, *J. Geophys. Res.*, **103**, 5513-5529, 1998.
- MacAyeal, D. R., E. Rignot, and C. L. Hulbe, Ice-shelf dynamics near the front of the Filchner-Ronne Ice Shelf, Antarctica, revealed by SAR interferometry: Model/interferogram comparison, *J. Glaciol.*, **44**, 419-428, 1998.
- Makinson, K., Residual tidal currents along Filchner-Ronne ice front, *Filchner-Ronne Ice Shelf Program Rep. 11*, pp. 36-41, Alfred-Wegener Inst., Bremerhaven, Germany, 1997.
- Makinson, K., and K. W. Nicholls, Modelling tidal currents beneath Filchner-Ronne Ice Shelf and on the adjacent continental shelf: Their effect on mixing and transport, *J. Geophys. Res.*, **104**, 13,449-13,467, 1999.
- Middleton, J. H., T. D. Foster, and A. Foldvik, Diurnal shelf waves in the southern Weddell Sea, *J. Phys. Oceanogr.*, **17**, 784-791, 1987.
- Nicholls, K. W., L. Padman, and A. Jenkins, First physical oceanography results from the ROPEX98 cruise to the southern Weddell Sea, *Filchner-Ronne Ice Shelf Program Rep. 12*, pp. 51-58, Alfred-Wegener Inst., Bremerhaven, Germany, 1998.
- Nøst, O. A., and S. Østerhus, Impact of grounded icebergs on the hydrographic conditions near the Filchner Ice Shelf, in *Ocean, Ice, and Atmosphere: Interactions at the Antarctic Continental Margin*, *Antarct. Res. Ser.*, vol. 75, edited by S. S. Jacobs and R. F. Weiss, pp. 267-284, AGU, Washington, D.C., 1998.
- Padman, L., and C. Kottmeier, High frequency ice motion and divergence in the Weddell Sea, *J. Geophys. Res.*, **105**, 3379-3399, 2000.
- Padman, L., R. A. Robertson, and K. W. Nicholls, Modelling tides in the southern Weddell Sea: Updated model with new bathymetry from ROPEX, *Filchner-Ronne Ice Shelf Program Rep. 12*, pp. 65-73, Alfred-Wegener Inst., Bremerhaven, Germany, 1998.
- Padman, L., K. W. Nicholls, and R. A. Woodgate, The 1998 Ronne Polynya Experiment (ROPEX), *Antarct. J. U. S.*, in press, 2000.
- Parke, M. E., R. H. Stewart, D. L. Farliss, and D. E. Cartwright, On the choice of orbits for an altimetric satellite to study ocean circulation and tides, *J. Geophys. Res.*, **92**, 11,693-11,707, 1987.
- Riedel, B., U. Nixdorf, M. Heinert, A. Eckstaller, and C. Mayer, The response of the Ekström Ice Shelf in the grounding zone to tidal forcing, *Ann. Glaciol.*, in press, 2000.
- Rignot, E., Tidal flexure, ice velocities and ablation rates of Petermann Gletscher, Greenland, *J. Glaciol.*, **42**, 476-485, 1996.
- Rignot, E., Radar interferometry detection of hinge-line migration on Rutford Ice Stream and Carlson Inlet, Antarctica, *Ann. Glaciol.*, **27**, 25-32, 1998a.
- Rignot, E., Fast recession of a West Antarctic glacier, *Science*, **281**, 549-551, 1998b.
- Rignot, E., and D. R. MacAyeal, Ice-shelf dynamics near the front of the Filchner-Ronne Ice Shelf, Antarctica, revealed by SAR interferometry, *J. Glaciol.*, **44**, 405-418, 1998.
- Robertson, R. A., L. Padman, and G. D. Egbert, Tides in the Weddell Sea, in *Ocean, Ice, and Atmosphere: Interactions at the Antarctic Continental Margin*, *Antarct. Res. Ser.*, vol. 75, edited by S. S. Jacobs and R. F. Weiss, pp. 341-369, AGU, Washington, D.C., 1998.
- Schlaax, M. G., and D. B. Chelton, Aliased tidal errors in TOPEX/Poseidon sea surface height data, *J. Geophys. Res.*, **99**, 24,761-24,775, 1994.
- Schrama, E. J. O., and R. D. Ray, A preliminary tidal analysis of TOPEX/Poseidon altimetry, *J. Geophys. Res.*, **99**, 24,799-24,808, 1994.
- Smithson, M. J., A. V. Robinson, and R. A. Flather, Ocean tides under the Filchner-Ronne Ice Shelf, Antarctica, *Ann. Glaciol.*, **23**, 217-225, 1996.
- Vaughan, D. G., J. Sievers, C. S. M. Doake, H. Hinze, D. R. Mantripp, V. S. Pozdeev, H. Sandhager, H. W. Schenke, A. Solheim, and F. Thyssen, Subglacial topography, ice thickness and water column thickness in the vicinity of the Filchner-Ronne ice shelf, *Z. Polarforsch.*, **64**, 75-88, 1994.
- Woodgate, R. A., M. Schröder, and S. Østerhus, Moorings from the Filchner Trough and the Ronne Ice Shelf Front: Preliminary results, *Filchner-Ronne Ice Shelf Program Rep. 12*, pp. 85-90, Alfred-Wegener Inst., Bremerhaven, Germany, 1998.

D. R. MacAyeal, Department of Geophysical Sciences, University of Chicago, 5734 S. Ellis Ave., Chicago, IL 60637. (drm7@midway.uchicago.edu)

L. Padman, Earth and Space Research, 1910 Fairview Avenue East, Suite 102, Seattle, WA 98102-3620. (padman@esr.org)

E. Rignot and M. Schmeltz, Jet Propulsion Laboratory, California Institute of Technology, MS 300-235, 4800 Oak Grove Drive, Pasadena, CA 91109. (eric@adelie.jpl.nasa.gov)

(Received May 19, 1999; revised November 11, 1999; accepted December 28, 1999.)